

Title	Luminescent optical detection of volatile electron deficient compounds by conjugated polymer nanofibers
Authors	Wade, Aidan; Lovera, Pierre; O'Carroll, Deirdre; Doyle, Hugh; Redmond, Gareth
Publication date	2015-03-24
Original Citation	WADE, A., LOVERA, P., O'CARROLL, D., DOYLE, H. & REDMOND, G. 2015. Luminescent optical detection of volatile electron deficient compounds by conjugated polymer nanofibers. Analytical Chemistry, 87, 4421-4428. doi: 10.1021/acs.analchem.5b00309
Type of publication	Article (peer-reviewed)
Link to publisher's version	10.1021/acs.analchem.5b00309
Rights	© 2015 American Chemical Society. This document is the Accepted Manuscript version of a Published Work that appeared in final form in Analytical Chemistry (copyright © American Chemical Society) after peer review and technical editing by the publisher. To access the final edited and published work see <a href="http://dx.doi.org/10.1021/acs.analchem.5b00309">http://dx.doi.org/10.1021/acs.analchem.5b00309</a>
Download date	2024-05-04 22:41:44
Item downloaded from	<a href="https://hdl.handle.net/10468/2457">https://hdl.handle.net/10468/2457</a>



# UCC

**University College Cork, Ireland**  
 Coláiste na hOllscoile Corcaigh

# Luminescent Optical Detection of Volatile Electron Deficient Compounds by Conjugated Polymer Nanofibers

Aidan Wade,<sup>§</sup> Pierre Lovera,<sup>†</sup> Deirdre O'Carroll,<sup>‡</sup> Hugh Doyle,<sup>\*,†</sup> and Gareth Redmond<sup>\*,§</sup>

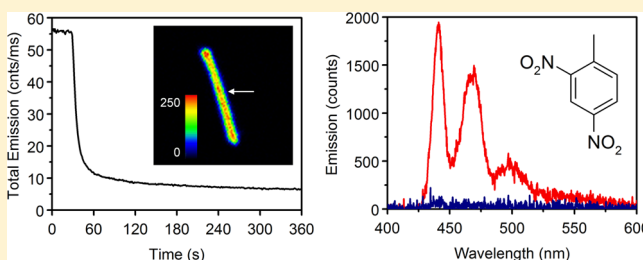
<sup>§</sup>School of Chemistry and Chemical Biology, University College Dublin, Belfield, Dublin 4, Ireland

<sup>†</sup>Tyndall National Institute, University College Cork, Lee Maltings, Cork, Ireland

<sup>‡</sup>Department of Materials Science and Engineering, Rutgers, The State University of New Jersey, 607 Taylor Road, Piscataway, New Jersey 08854, United States

**S** Supporting Information

**ABSTRACT:** Optical detection of volatile electron deficient analytes via fluorescence quenching is demonstrated using ca. 200 nm diameter template-synthesized polyfluorene nanofibers as nanoscale detection elements. Observed trends in analyte quenching effectiveness suggest that, in addition to energetic factors, analyte vapor pressure and polymer/analyte solubility play an important role in the emission quenching process. Individual nanofibers successfully act as luminescent reporters of volatile nitroaromatics at subparts-per-million levels. Geometric factors, relating to the nanocylindrical geometry of the fibers and to low nanofiber substrate coverage, providing a less crowded environment around fibers, appear to play a role in providing access by electron deficient quencher molecules to the excited states within the fibers, thereby facilitating the pronounced fluorescence quenching response.



Detection of trace amounts of electron deficient compounds is important for a number of applications including screening for hidden explosives, humanitarian demining, and environmental monitoring, as well as criminal and forensic investigations.<sup>1,2</sup> In recent years, due to the increasing threat from terrorism and organized crime, and the consequent demand for improved security for citizens and infrastructure, much attention has focused on detection of explosives such as nitroaromatics (TNT, TNB), nitramines (RDX, HMX, Tetryl), nitrate esters (PETN, nitrocellulose), and organic peroxides (TATP, HMTD). Molecules that are not explosive themselves, but present as impurities (DNT) or tags (DMNB) in common formulations, can also be target analytes. To detect explosives with high sensitivity and high selectivity, many detection methods have been explored, including gas chromatography, mass spectroscopy, ion mobility spectroscopy and trained canine teams.<sup>2–4</sup> However, these approaches are either bulky, expensive, or require time-consuming training and operation, limiting their deployment to fixed site screening at major transportation hubs or government buildings.<sup>5</sup> Optical addressed sensors have advantages in terms of sensitivity, speed, portability, and cost-effectiveness, as well as offering a variety of transduction schemes for signal retrieval.<sup>1,5</sup> Sensors for detection of explosive compounds have focused on colorimetric and fluorescence detection methods,<sup>6–8</sup> with a number of sensors based on organic and inorganic conjugated polymers, small molecule fluorophores, metallo-organic complexes, and molecularly imprinted polymers reported.<sup>6,9–14</sup> While each class of chemical explosives presents their own set

of challenges for detection, nitroaromatics present particular difficulties for gas phase sensors due to their low vapor pressures.<sup>15</sup> However, these electron deficient analytes bind strongly to the electron-rich polymer thin films typically used, while the subsequent fluorescence quenching response is amplified by the molecular wire configuration of the chromophores.<sup>14,16,17</sup> The Fido explosives sensing platform, based on this amplifying fluorescent polymers (AFP) approach, is capable of detecting a range of nitrated explosive vapors.<sup>18,19</sup> Although most optically addressed detectors have been based on planar transducer formats such as spun cast thin films or spotted arrays, one-dimensional (1D) nanostructures such as nanowires, nanotubes, and nanofibers have been attracting increasing attention as chemical and biological sensors.<sup>20–27</sup> Organic 1D nanostructures, possessing the processability and high photoluminescence (PL) efficiency of their constituent molecular components,<sup>28–30</sup> also offer advantages for sensing applications including their high surface-to-volume ratios and analyte diffusion into the organic matrix, which is more difficult for inorganic semiconductor nanowires or glass nanofibers.<sup>31,32</sup> The long-range exciton migration intrinsic to the well-organized molecular arrangement within these nanostructures magnifies the fluorescence quenching response to surface adsorbed analytes.<sup>10,17,33</sup>

**Received:** January 21, 2015

**Accepted:** March 24, 2015



Current strategies employed to enhance the sensitivity of 1D nanostructures for sensing applications are focused on the structure-level design by controlling the structure morphology.<sup>34,35</sup> The structures of various 1D nanomaterials, and their hierarchical assemblies including meshes and nanoarrays, effectively influence the absorption and diffusion behaviors of the analyte.<sup>18,36,37</sup> Therefore, considerable efforts have been placed on optimizing the 1D structures and assemblies to achieve high sensitivity, selectivity and fast time response.<sup>38</sup> Besides tailoring the morphology and size of the nanostructures, binary and multicomponent materials have investigated to achieve superior sensing performance.<sup>39</sup> Doping is commonly used to achieve controlled changes to photophysical characteristics and consequent enhancements of sensing performance.<sup>34</sup> The composite nanostructures can not only combine the properties of different compounds but also generate new functionality based on intermolecular interactions and energy transfers.<sup>40,41</sup> In this article, we report on the luminescent optical detection of volatile electron deficient compounds by conjugated polymer nanofibers based on poly(9,9-dioctylfluorenyl-2,7-diyl), (PFO). The performance of dense arrays of luminescent PFO nanofibers for gas phase detection of trace amounts of 2,4-dinitrotoluene (DNT), anthraquinone (AQ), and duroquinone (DQ) analytes was compared with that of a thin film based sensor format prepared using the same parent material. Following this, the effect of packing density on the fluorescence quenching response is investigated. Finally, detection of nitroaromatics at subparts-per-million levels is demonstrated on individual nanofibers by scanning confocal microscopy and photoluminescence spectroscopy.

## EXPERIMENTAL METHODS

**Materials.** Porous alumina membranes with nominal pore diameters of 200 nm were purchased from Whatman Ltd. Poly(9,9-dioctylfluorenyl-2,7-diyl), PFO, with a polydispersity index of 3.0 and a weight-average of 100 000 (PS standards) was purchased from H.W. Sands Corp. Sulfuric acid (H<sub>2</sub>SO<sub>4</sub>; 95–98%), sodium hydroxide, anhydrous tetrahydrofuran (THF), chloroform (CHCl<sub>3</sub>), hydrochloric acid (HCl; 37% in water), methanol, acetone, decane, 2,4-dinitrotoluene (2,4-DNT; 97%), duroquinone (DQ; 97%), and anthraquinone (AQ; 98%) were purchased from Sigma-Aldrich, Ltd. All reagents and solvents were used without further purification. Deionized water (>16.1 MΩ cm, Milli-Q, Millipore) was used for all aqueous solutions.

**Preparation of Polyfluorene Nanofibers.** A concentrated solution of PFO (60 mg/mL) was prepared by dissolving the polymer in anhydrous THF in a sealed amber glass vial, while heating to 60 °C and stirring vigorously for 30 min. The solution was allowed cool to room temperature. Alumina membranes were sonicated in methanol and air-dried prior to use. A 50 μL drop of polymer solution was deposited on top of a membrane. A glass coverslip was placed on top of the drop, facilitating penetration of the solution into the template pores. A weight of ca. 2.5 kg was applied overnight. Following this, excess material was removed from the template surface by scraping with a razor blade. The template, with embedded nanofibers, was soaked in aqueous NaOH (3 M) for 12 h to dissolve the alumina host. The NaOH solution was removed and the nanofiber residue was gently washed three times with deionized water and once with acetone before finally dispersing the fibers in decane (with sonication for ca. 2 s). Random arrays

of nanofibers were prepared by depositing 5 μL droplets of fibers, suspended in decane, onto clean glass coverslips followed by drying overnight in air.

**Imaging and Optical Measurements.** Scanning electron microscopy (SEM) images were acquired using a field emission instrument (FEI Quanta 3D DualBeam SEM, FEI) operating at beam voltages of 1–10 kV. Atomic force microscopy (AFM) images were acquired in tapping mode using a calibrated instrument (Innova, Bruker AXS) with commercial tapping mode probes (typical radius of curvature ca. 8 nm, front/side cone angles of 15 ± 2°/17.5 ± 2° respectively and nominal spring constant of 20–80 N/m; MPP-11123-10, Bruker AXS). No processing was applied to data apart from background plane subtraction. Luminescence microscopy images were acquired using an upright epi-fluorescence microscope (BX51, Olympus) equipped with a 100 W halogen lamp and a thermoelectrically cooled color CCD camera (Fast1394 QICAM, QImaging). UV–vis absorption spectra were acquired using a double-beam spectrophotometer (V-650, Jasco) equipped with an optional 60 mm integrating sphere (ISV-722, Jasco). Photoluminescence (PL) spectra were recorded using a luminescence spectrometer equipped with a pulsed Xe short arc discharge lamp and Czerny–Turner monochromators (QuantaMaster 40, Photon Technology International).

**PL Emission Quenching Studies.** The emission quenching response of PFO thin films and nanofiber arrays to vapors of electron deficient analytes was ascertained by inserting one such sample at a time into a sealed quartz cuvette containing solid 2,4-DNT, DQ, or AQ at room temperature. The analyte material had been presealed in the cuvette for 1 h in advance in order to allow it reach its equilibrium vapor pressure. After a certain time period had elapsed, the PFO sample was removed from the cuvette and a PL spectrum was immediately recorded. Thin film and nanofiber samples (on coverslips) were mounted at 45° to the incident beam using a home-built coverslip holder in a quartz cuvette that was placed into the cuvette holder of the QuantaMaster 40 system. The solid quencher was placed at the bottom of the cuvette to avoid direct contact with the polymer sample on the coverslip. As a result, only vapors from the analyte interacted with the PFO polymer sample. Single nanofiber emission measurements were carried out using a scanning confocal PL microscope (MicroTime 200, PicoQuant GmbH) equipped with a 402 nm pulsed picosecond laser diode.

## RESULTS AND DISCUSSION

**Polyfluorene Nanofibers.** PFO nanofibers were prepared under ambient conditions via solution-assisted wetting of porous anodized alumina membrane templates. Following synthesis, the nanofiber-filled template was attached to an adhesive carbon pad and the alumina host was selectively dissolved in aqueous NaOH (3 M). The remaining nanofibers were rinsed with deionized water and dried under nitrogen gas flow. Scanning electron microscopy (SEM) images of a freestanding PFO nanofiber array following selective removal of the template are shown in Figure 1a and b. The data demonstrate that close-packed forests of nanofibers were formed (~10<sup>9</sup> nanofibers/cm<sup>2</sup>). Statistical analysis of the SEM image data indicated a mean nanofiber diameter of 208 ± 30 nm, in good agreement with the nominal template pore diameter; see Figure 1c. The fibers exhibited a smooth outer surface morphology without obvious structural defects.



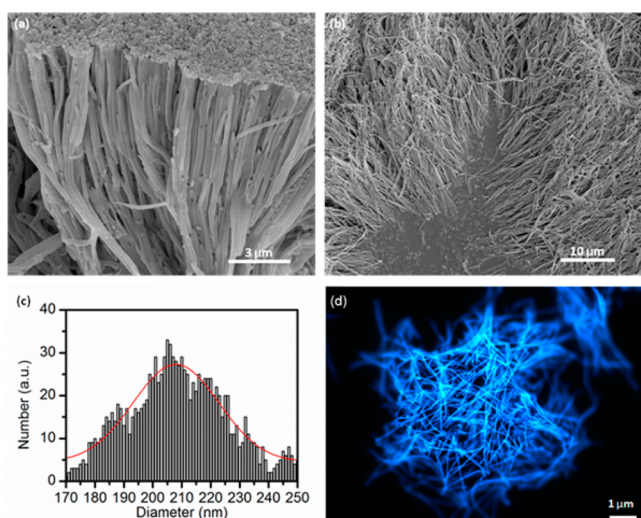


**Figure 1.** (a and b) Scanning electron microscopy images of a “forest” of nanofibers following selective dissolution of the alumina template. (c) Histogram of nanofiber diameters obtained following SEM image analysis. The solid red line is a Gaussian fit to the diameter distribution. (d) Epi-fluorescence image of a random PFO nanofiber array on a glass substrate.

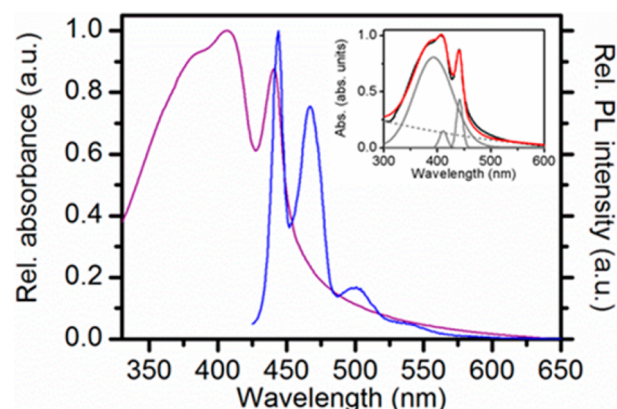


**Figure 2.** Intensity-normalized absorption (mauve line) and emission (blue line) spectra ( $\lambda_{\text{ex}}$ : 407 nm) of a random array of PFO nanofibers deposited on a glass substrate. (inset) Plot of three Gaussian functions (solid gray lines) and a background Gaussian function (dashed gray line) that were fitted to the nanofiber array absorption spectrum (solid black line). The sum of all four Gaussians is shown (red line).

algorithm; see Figure 2, inset.<sup>46</sup> An additional Gaussian was fit to the data to account for the background signal, mainly due to optical scattering from the nanofiber array. The amount of  $\beta$ -phase was estimated by dividing the combined area of the Gaussians centered at 407 and 441 nm by the total area of all the fitted Gaussians (neglecting the contribution from the long wavelength tail). An upper limit value for the  $\beta$ -phase fraction of 7% was determined.<sup>47</sup>

Overall, the spectroscopic data indicated that a fraction of the amorphous phase PFO molecules, with initially random molecular chain conformations, had adopted the more planar and extended  $2_1$  helical molecular conformation of the  $\beta$ -phase during synthesis;<sup>48</sup> see Scheme SI.3, Supporting Information. The nanofiber emission spectra were completely dominated by this fraction, due either to Förster-type energy transfer or to singlet exciton migration from the glassy phase to the lower energy  $\beta$ -phase.<sup>43,45,49</sup> Formation of the  $\beta$ -phase within polymer fibers was attributed to the action of mechanical stresses that arose during solution-assisted filling of the alumina template pores and, afterward, during solvent evaporation.<sup>42,50</sup>

**PL Quenching of Films and Nanofiber Arrays.** The photoluminescence behaviors of  $\beta$ -phase containing PFO thin films and nanofibers in the presence of vapors of an electron deficient analyte were compared by exposing individual samples to solid analyte material (that was presealed in cuvettes for 1 h in advance in order to allow the analyte reach its equilibrium vapor pressure) for specific periods of time prior to measuring PL spectra. PL spectra acquired for a typical, ca. 6.5 nm thick,  $\beta$ -phase containing PFO film on a glass substrate following exposure to DQ vapors for 0, 10, 30, 60, 120, 180, 300, and 600 s, respectively, are shown in Figure 3a. For comparison, PL spectra acquired under identical conditions for a typical dense, random array of PFO nanofibers on a glass substrate are shown in Figure 3b. As expected, both film and nanofiber spectra were dominated by  $\beta$ -phase emission. Additionally, exposure to DQ vapors resulted in a marked and rapid quenching of both film and nanofiber emission. The time dependence of the quenching responses, determined by monitoring the intensity of the 0–1 emission peaks (centered at 467 nm) as a function of exposure time indicated a decrease in film emission intensity of 73% after 10 s, which progressed to 86% after 60 s. In contrast, nanofiber array emission responded more gradually during exposure to

An epi-fluorescence microscopy image of a dense array of nanofibers that was deposited onto a glass substrate from a decane suspension is shown in Figure 1d. Nanofiber length,  $L$ , was found to range between 2 and 40  $\mu\text{m}$ , and mean fiber length was found to be  $15 \pm 2 \mu\text{m}$ . Some degree of radial curvature was observed for the majority of the fibers, indicating the flexibility of these nanostructures. Uniform blue photoluminescence with a low emission background was observed along the full lengths of the fibers, indicating that the nanofiber formation and extraction protocols provided dispersions of robust, discrete high-aspect ratio PFO nanofibers in a format suitable for deposition of nanofiber arrays. Additionally, the density of the deposited arrays could be readily tuned from dense, multilayer surface coverage to well-dispersed, submonolayer surface coverage by appropriate dilution of the nanofiber suspension.

Typical intensity-normalized absorption and PL spectra acquired for a random PFO nanofiber array on glass are shown in Figure 2. The absorption spectrum of the nanofiber array exhibited a band at ca. 395 nm (fwhm of ca. 110 nm) with a shoulder near 407 nm and a pronounced low energy peak at 441 nm, the latter features being characteristic of the  $S_0 \rightarrow S_1$  0–1 and 0–0 transitions of  $\beta$ -phase PFO, respectively, and indicated that a fraction of  $\beta$ -phase chains had formed within the amorphous phase matrix of the PFO nanofibers.<sup>42,43</sup> The long wavelength tail in this spectrum (above 450 nm) was attributed to a degree of optical scattering by the nanofiber array.<sup>44</sup> The PL spectrum of the nanofiber array exhibited comparatively narrow emission peaks (viz. the PL spectrum of an as-spun PFO thin film shown in Figure SI.1, Supporting Information) at 441, 467, and 500 nm, indicative of a narrowed distribution of emitting PFO chain segments with increased effective conjugation lengths. This spectrum was characteristic of the  $S_1 \rightarrow S_0$  0–0 transition, with associated vibronic replicas, of  $\beta$ -phase PFO.<sup>42,45</sup>

The fraction of  $\beta$ -phase material present within the fibers was estimated by deconvoluting the absorption spectrum by fitting it with three Gaussian functions using a nonlinear least-squares

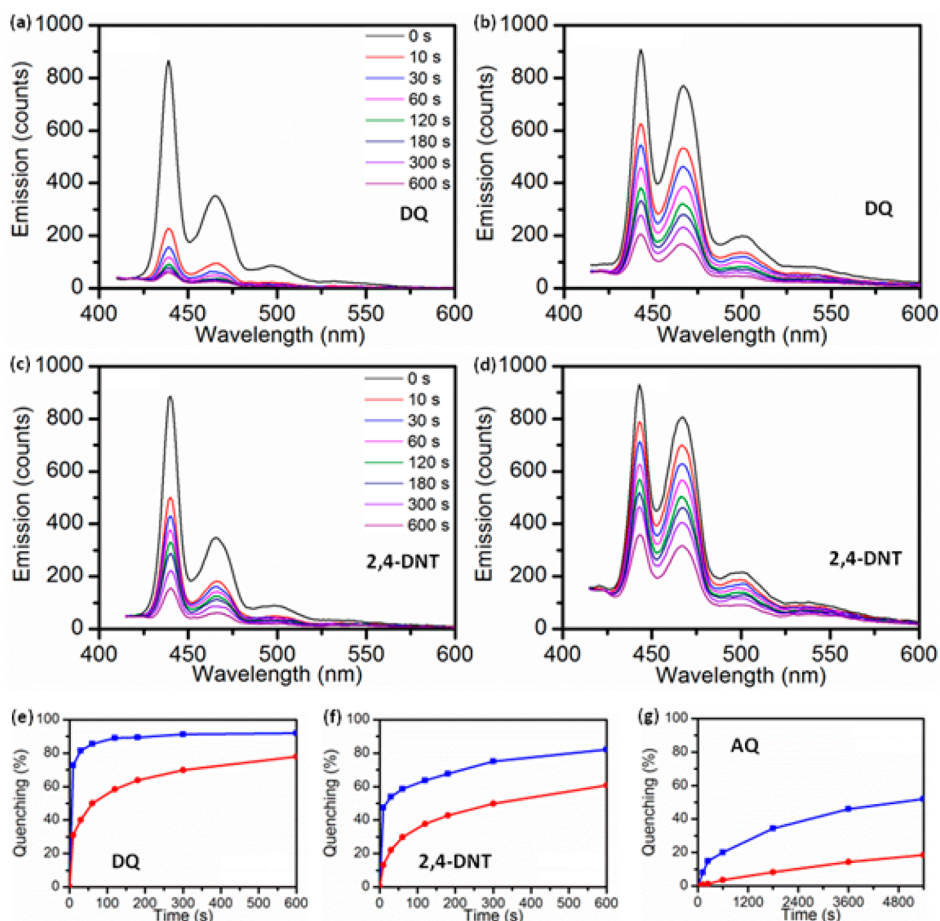


**Figure 3.** (a) PL spectra recorded for a typical  $\beta$ -phase containing PFO thin film on exposure to DQ vapor for different times. (b) Analogous data measured for a typical dense, random array of PFO nanofibers. (c) PL spectra recorded for a thin film on exposure to 2,4-DNT vapor for different times. (d) Analogous data measured for a dense nanofiber array. (e–g) Extent of PL quenching (decay of 0–1 peak intensity) for film (blue lines) and nanofiber array (red lines) samples as a function of exposure to DQ, 2,4-DNT, and AQ, respectively. Note: for all,  $\lambda_{\text{ex}} = 401$  nm.

DQ vapor, with a decrease in nanofiber emission intensity of 31% after 10 s, which progressed to 50% after 60 s; see Figure 3e.

PL spectra acquired for a typical  $\beta$ -phase containing PFO film following exposure to 2,4-DNT vapors are shown in Figure 3c. For comparison, PL spectra acquired under identical conditions for a typical dense, random array of PFO nanofibers are shown in Figure 3d. Exposure to 2,4-DNT vapors resulted in rapid emission quenching. The quenching responses indicated a decrease in film emission intensity of 48% after 10 s, which progressed to 59% after 60 s. Again, nanofiber array emission responded more gradually, with a decrease in fiber emission intensity of 13% after 10 s, which progressed to 30% after 60 s; see Figure 3f. Finally, the time dependent quenching responses observed for a  $\beta$ -phase containing PFO film and a dense, random array of PFO nanofibers following exposure to AQ vapors are compared in Figure 3g. Exposure to AQ vapors resulted in a notably slow quenching of emission. A decrease in film emission intensity of 4% after 10 s, which progressed to 5% after 60 s, was observed, while nanofiber emission intensity decreased by 2% after 10 s and progressed to only 3% after 60 s.

**PL Quenching Mechanism and Trends.** Since the wavelength range of the PFO emission was far above the absorption range of the analytes (see Figure SI.5, Supporting Information), emission quenching by excited state energy transfer was considered unlikely. Therefore, the observed

quenching response was assigned to photoinduced electron transfer from the excited PFO to the electron deficient analytes. The overall free energy change,  $\Delta G^\circ$ , may be approximated by

$$\Delta G^\circ = E(\text{P}/\text{P}^{+\bullet}) - \Delta E_{0-0} - E(\text{Q}/\text{Q}^{+\bullet})$$

where  $E(\text{P}/\text{P}^{+\bullet})$ ,  $\Delta E_{0-0}$ , and  $E(\text{Q}/\text{Q}^{+\bullet})$  are the oxidation potential of the PFO polymer, the lowest singlet 0–0 excitation energy of the polymer and the reduction potential of the analyte, respectively.<sup>51</sup>  $E(\text{P}/\text{P}^{+\bullet})$  and  $\Delta E_{0-0}$  values for glassy phase PFO are 1.6 V (vs SCE)<sup>52</sup> and 2.90 eV, respectively.  $E(\text{Q}/\text{Q}^{+\bullet})$  values for 2,4-DNT, AQ, and DQ are –1.0, –0.9, and –0.8 V (vs SCE), calculated from various different electrochemical and optical measurement data; see Table SI.1, Supporting Information.<sup>53–57</sup> This results in  $\Delta G^\circ$  values between –0.30 and –0.50 eV; see Scheme SI.4, Supporting Information, for a schematic of the oxidative electron transfer process.

The uptake,  $M(t)$ , of an analyte by a thin film over a given exposure time period can be calculated by

$$M(t) = 2M(\infty) \sqrt{\frac{Dt}{\pi L^2}}$$

where  $D$  is the diffusion coefficient of the analyte within the film,  $M(\infty)$  is the mass uptake at the equilibrium point, taken as  $SV$  where  $S$  is the solubility of the analyte within the film and



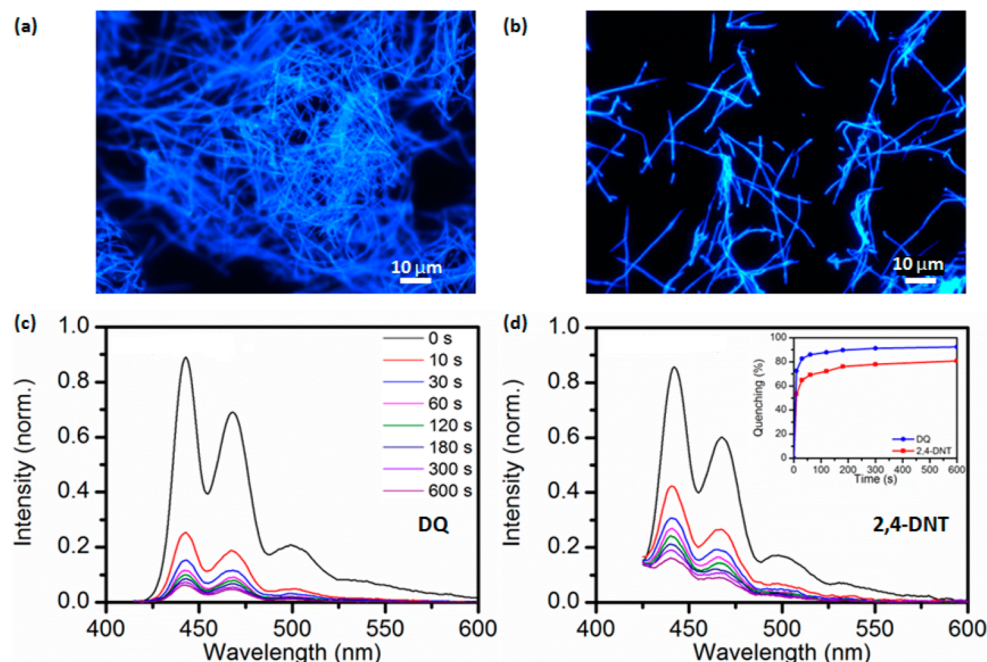


**Figure 4.** (a and b) Representative epi-fluorescence microscopy images of dense and disperse random nanofiber arrays, respectively. (c and d) Emission spectra ( $\lambda_{\text{ex}}$ : 401 nm) recorded for typical disperse nanofiber arrays on exposure to DQ and 2,4-DNT vapors, respectively, for different times. (inset) Extent of emission quenching (decay of 0–1 peak intensity) during exposure to DQ (blue) and 2,4-DNT (red), respectively.

$V$  its volume,  $L$  is the film thickness (cm), and  $t$  is the total exposure time.<sup>58</sup> To estimate the uptake of, e.g., 2,4-DNT by a PFO thin film, mean values of  $D$  ( $1.1 \times 10^{-9}$  cm<sup>2</sup>/s) and  $S$  ( $29 \times 10^{-6}$  g/cm<sup>3</sup>) for 2,4-DNT were obtained for five different polymers with comparable diffusivity and solubility to PFO.<sup>59</sup>

Given that the PFO films were 2.42 cm<sup>2</sup> in area and 6.5 nm in thickness, the total 2,4-DNT uptake after 18 s (ca. 50% emission quenching) was estimated to be ca.  $1.0 \times 10^{-8}$  g or  $5.9 \times 10^{-11}$  mol. The total amount of PFO polymer within the film was ca.  $1.57 \times 10^{-6}$  g (bulk PFO density of ca. 1 g cm<sup>-3</sup> without compression)<sup>43</sup> giving a total number of 9,9-dioctylfluorenyl monomers of ca.  $5 \times 10^{-9}$  M. Consequently, the molar ratio of uptaken 2,4-DNT molecules to the total number of available emissive fluorene monomers was about 1:85, indicating that emission quenching likely occurred via an amplified luminescence quenching process mediated by PFO polymer chains (which permitted exciton migration within the film) rather than via direct quencher analyte–chromophore interaction.<sup>60</sup> Since the film thickness was on the order of the exciton migration range (0–5 nm) measured for amorphous PFO,<sup>60</sup> this amplified quenching process facilitated effective quenching of film emission with a 2,4-DNT exposure time of only a few minutes.

While a strong, negative exergonicity ( $\Delta G^\circ$ ) facilitates emission quenching, the quenching rate (EQ) is also related to the polymer–analyte binding strength ( $K_b$ ) and the vapor pressure of the quenching analyte molecules (VP) by the expression  $\text{EQ} \propto [\exp(-\Delta G^\circ)^2] K_b \text{VP}$ .<sup>10</sup> This is pertinent to the present study since the quenching effectiveness of the analytes above (DQ > 2,4-DNT > AQ) differed from the relative magnitudes of the reaction exergonicities (DQ > AQ > 2,4-DNT); see Figure 3e–g. While it was not possible to obtain exact values for the polymer–analyte binding constants ( $K_b$ ), polymer–analyte interactions may be considered in terms of the free energy of mixing, i.e.,  $\Delta G_M = \Delta H_M - T\Delta S_M$ .<sup>61</sup>  $\Delta H_M$  may be estimated from  $\Delta H_M = \Phi_A \Phi_P (\delta_A - \delta_P)^2$ , where  $\Phi_A$  and  $\Phi_P$

are the volume fractions of analyte and polymer, respectively, and  $\delta_A$  and  $\delta_P$  are the corresponding solubility parameters.<sup>61</sup> Since a negative  $\Delta G_M$  is required for solubility,  $\Delta H_M$  and  $(\delta_A - \delta_P)^2$  (i.e.,  $\Delta\delta$ ) should be as small as possible. The Hansen solubility parameters for PFO and the analytes<sup>61</sup> were used to estimate  $\Delta\delta$  for each of the three polymer/analyte pairs; see Tables SI.2 and SI.3 of the Supporting Information.

Qualitatively, for  $\Delta\delta < 1$  analyte and polymer are expected to be miscible, for  $\Delta\delta = 1$  the components will be partially miscible, and for  $\Delta\delta > 1$  the components will become progressively immiscible.<sup>62</sup> Importantly, the order of the magnitudes of the  $\Delta\delta$  values estimated for each of the three polymer/analyte pairs was consistent with their observed quenching effectiveness. The role of the vapor pressure of the analyte molecules (VP) in influencing EQ was also considered. Again, the relative magnitudes of the equilibrium vapor pressures were consistent with the observed order of quenching effectiveness. The more effective PFO quenching response was observed in the presence of DQ, with a vapor pressure of DQ ( $2.88 \times 10^{-3}$  mm Hg, or 2324 ppb, at 25 °C), followed by 2,4-DNT ( $1.47 \times 10^{-4}$  mm Hg, or 118 ppb, at 25 °C) and AQ ( $1.16 \times 10^{-7}$  mm Hg, or 0.1 ppb, at 25 °C), respectively.<sup>63</sup>

**Role of Sample Morphology.** From consideration of Figures 3e–g, it is apparent that the EQ for each of the analytes was greater for the ca. 6.5 nm thick  $\beta$ -phase containing PFO thin films than for the PFO nanofiber arrays. Concerning the morphology of the latter samples, dense nanofiber arrays were typically observed to comprise multilayers of nanofibers distributed in randomly stacked, disorganized arrangements; see Figure 4a. To probe the effect of nanofiber density and substrate surface coverage on the emission quenching response of the arrays, lower density nanofiber arrays were prepared using a diluted ( $\times 4$ ) nanofiber/decane suspension; see Figure 4b. PL spectra acquired of disperse nanofiber arrays, comprised of submonolayers of disperse, randomly distributed nanofibers on glass substrates, following exposure to DQ or 2,4-DNT

vapors are shown in Figure 4c and d, respectively. Exposure to the DQ and 2,4-DNT vapors resulted in a prompt and significant quenching of nanofiber array emission. The time dependence of the quenching responses, determined by monitoring the intensity of the 0–1 emission peaks (at ca. 467 nm) as a function of duration of exposure to DQ vapor, indicated a decrease in disperse nanofiber array emission intensity of 73% after 10 s, which progressed to 87% after 60 s; see Figure 4d, inset. While exposure to 2,4-DNT vapor resulted in slightly less pronounced emission quenching, the time-dependent quenching responses indicated a decrease in disperse nanofiber array emission intensity of 53% after 10 s, which progressed to 69% after 60 s. Therefore, the emission quenching responses of disperse PFO nanofiber arrays were markedly improved over the responses measured for dense nanofiber arrays and were very similar to those measured for  $\beta$ -phase containing PFO thin films; see Figure 3e and f. Specifically, the emission quenching responses to DQ vapor were practically identical for thin films and disperse fiber arrays (extent of array quenching at 60 s/extent of film quenching at 60 s = 87%/86% = 1.01) while the responses measured during exposure to 2,4-DNT vapor were slightly more pronounced for nanofiber arrays than for thin films (extent of array quenching at 60 s/extent of film quenching at 60 s = 69%/59% = 1.17). The observation that disperse arrays of ca. 200 nm diameter PFO nanofibers could act as luminescent reporters of the selected volatile electron deficient compounds and that, during exposure to these analyte vapors, they exhibited an emission quenching response which was comparable to that of the ca. 6.5 nm thick PFO films (see Figure SI.5, Supporting Information), was very encouraging since the greater thickness of the fibers might have been expected to reduce their relative response. In this regard, assuming similar porosities and polymer–analyte interactions for the solution processed PFO films and nanofibers, a slower quenching response could be plausibly expected for the fibers as a result of the longer times that might be required for analyte molecules to diffuse into the interior of the material during the quenching process.

However, the improved emission quenching performance observed for the disperse nanofiber arrays suggested that geometric factors relating to the lower substrate coverage, providing a less crowded environment around each of the fibers, may play a role in the quenching response. Specifically, the cylindrical geometry of the disperse, randomly distributed fibers may offer a significant advantage over planar thin films for vapor detection, as sensor size and shape are known to deeply affect the time required to capture a given number of analyte molecules. For example, for a hemicylindrical sensor, it has been shown that the time required to accumulate analyte molecules on the sensor surface via static diffusion is significantly shorter than that required for a disk-shaped sensor.<sup>64</sup> Likewise, it has been predicted, and experimentally confirmed, that the response time for moisture diffusion into a cylindrical polymer sensor structure may be up to 10-fold shorter than that for a thin film sensor of identical thickness and composition.<sup>65</sup>

Although a trade-off does exist between the average response time and minimum concentration of analyte molecules that is detectable by a sensor operating in a diffusion-limited regime, it has been shown that, for the same response times, the detection limit of a nanofiber sensor may still be 3–4 orders of magnitude higher than that of a planar sensor.<sup>66</sup> These observations justify the use of nanofibers in certain sensing applications and, for the

PFO nanofibers employed in this work, the geometric factors associated with the disperse nanofiber arrays likely facilitated access by the electron deficient quencher molecules to the excited states within the fibers enabling prompt quenching responses.

**Single Nanofiber PL Quenching.** Further studies were carried out on individual PFO nanofibers in order to explore the ultimate level of miniaturization attainable for this nanofiber based sensor format. To this end, single nanofiber optical measurements were undertaken using a time-resolved laser scanning confocal photoluminescence microscopy and spectroscopy system; see Figure 5. In a typical experiment, a

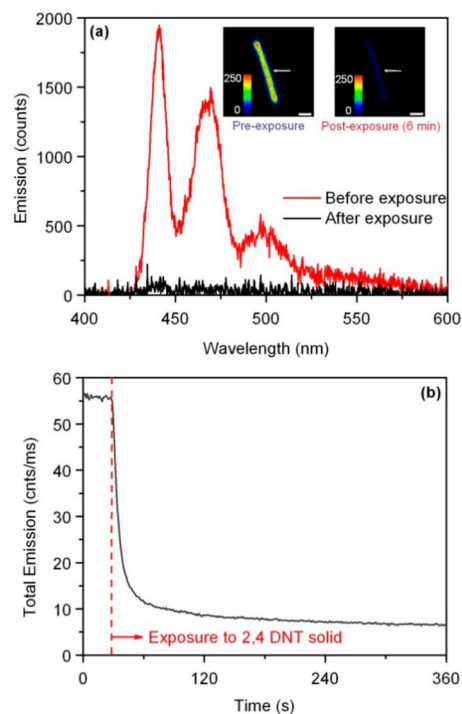


**Figure 5.** (a) PL spectra recorded for a single nanofiber before and after exposure to a nearby solid 2,4-DNT pellet. (inset) Scanning confocal emission intensity images of the fiber before and after exposure; arrows indicate the location at which data were acquired. (b) Emission intensity versus time trace measured for the nanofiber prior to and during exposure to the 2,4-DNT material. Note: for all,  $\lambda_{\text{ex}}$  = 402 nm.

scanning confocal emission intensity image and a location specific PL spectrum ( $\lambda_{\text{ex}}$ : 402 nm) were first recorded for a selected nanofiber on a glass substrate under ambient conditions. To prevent photobleaching, data were recorded quickly (images: 2 ms pixel integration time; spectra: 30 s integration time) at an incident excitation power <0.1 nW/cm<sup>2</sup>. Then, to ensure that the nanowire emission output was stable, the integrated emission intensity ( $\lambda > 430$  nm) was recorded in real time for 30 s at which point a solid pellet of 2,4-DNT material (51 mg) was gently placed into position at a height of 5 mm above the nanofiber sample; see Scheme SI.2, Supporting Information. The nanofiber emission intensity was subsequently recorded over a period of ca. 6 min. Following this, a second scanning confocal emission intensity image and spectrum were recorded for the fiber. Emission intensity images of a typical selected nanofiber that were recorded prior to and following exposure to 2,4-DNT in this manner are

shown in the inset to Figure 5. The nanofiber exhibited a 10-fold decrease in emission intensity that was uniform along the full length of the fiber, i.e., no residual emission “hot spots” were observed. Corresponding PL spectra measured at a location on the nanofiber before (black line) and after (red line) exposure are shown in the main panel of Figure 5a. Clearly, exposure resulted in an almost complete quenching of the nanofiber emission. (Note that the apparent slight red shift in the wavelength position of the 0–0 emission peak was an artifact caused by the low transmission of the 430 nm long pass filter.)

Finally, the emission intensity versus time trace was acquired at the same location on the nanofiber; see Figure 5b. Prior to placement of the 2,4-DNT material near the nanofiber, a stable emission trace, with an average intensity of ca. 55 counts/ms, was recorded. Immediately following placement, as 2,4-DNT molecules volatilized from the surface of the solid sample, entered the ambient atmosphere and diffused toward the nanofiber, a dramatic decrease in nanofiber emission intensity was observed. Under these conditions, the local concentration of 2,4-DNT molecules in the vicinity of the nanofiber was expected to be considerably less than that obtained using the cuvette approach (i.e., equilibrium vapor pressure) employed during the thin film and nanofiber array measurements described above. Remarkably, for the single nanofiber, emission was observed to rapidly drop by ca. 10% after only 1 s, by 50% after 6 s, and by ca. 82% after 60 s. The good agreement observed between data obtained during multiple measurements at different locations along different fibers confirmed that the reduction in nanofiber emission intensity were due to analyte-induced emission quenching and not to localized photo-bleaching. To estimate the vapor pressure of 2,4-DNT molecules at the nanofiber surface, an approximation in terms of diffusion from a planar surface using Fick’s law, made by considering that the pellet dimensions were substantially greater than those of the nanofiber, was used:

$$\frac{\partial \phi}{\partial t} = D \frac{\partial^2 \phi}{\partial x^2}$$

where  $D$  is the 2,4-DNT diffusivity in air ( $0.203 \text{ cm}^2/\text{s}$ )<sup>67</sup> and  $\phi$  is the flux of 2,4 DNT molecules. The resulting 1D solution is

$$\phi(x, t) = \phi(0, 0) \operatorname{erfc}\left(\frac{x}{2\sqrt{Dt}}\right)$$

Using this, and assuming that  $\phi(0,0)$  is proportional to the saturation vapor pressure of 2,4-DNT (140 ppb at 25 °C),<sup>63</sup> the vapor pressure at the surface of the nanofiber array sample 1 s after placement of the pellet was estimated to be 25 ppb. Assuming this represents the detection limit of the nanofiber sensor, this compares very well with current commercially available explosive sensors.<sup>18,19</sup>

## CONCLUSION

The photoluminescence behavior of PFO nanofiber arrays changes markedly in the presence of vapors of electron deficient analytes, which cause significant quenching of nanofiber emission via an amplified luminescence quenching process. The observed order of analyte quenching effectiveness is  $\text{DQ} > \text{2,4-DNT} > \text{AQ}$  indicating that, in addition to energetic factors, analyte vapor pressure and polymer/analyte solubility plays an important role in the emission quenching process. Examination of the emission quenching responses of

submonolayers of disperse, randomly distributed nanofibers, permits detection of nitroaromatics at subppm levels by individual nanofibers. The observation that individual ca. 200 nm diameter PFO nanofibers exhibit an emission quenching response competitive with that of ca. 6.5 nm thick PFO films, suggests that geometric factors relating to the lower nanofiber substrate coverage, providing a less crowded environment around the fibers, combined with the nanocylindrical fiber geometry, play a role in providing access by the electron deficient quencher molecules to the excited states within the fibers thereby facilitating the quenching response.

The results confirm that such nanostructures may successfully act as luminescent nanoscale vapor sensors and demonstrate the performance that may be achieved by controlling the structure and morphology of sensor transducer elements at the nanoscale. Practical application of the PFO nanofibers for volatile compound sensing requires a portable, cost-effective device with full data connectivity for field operations.<sup>68</sup> Ozcan and co-workers demonstrated fluorescent imaging of single nanoparticles, viruses, and DNA fragments on a smartphone-based optical reader,<sup>69,70</sup> which was later used for detection of parts-per-billion level detection of mercury contamination in real world water samples.<sup>71</sup> More recently, Ming et al. reported the development of low-cost chip-based wireless multiplex diagnostic device using a smartphone-based optical reader.<sup>72</sup> The excellent responsivity and signal-to-noise ratios exhibited by the PFO nanofibers lend themselves to this smartphone based approach for realization of an optical sensor platform, with rapid response times and subparts-per-million detection levels.

## ASSOCIATED CONTENT

### Supporting Information

Further experimental details. Characteristics of PFO thin films and their luminescence responses to analytes. Key physical parameters of the conjugated polymer/analyte system. Comparative quenching responses of PFO thin films, nanofiber arrays, and single nanofibers. This material is available free of charge via the Internet at <http://pubs.acs.org>.

## AUTHOR INFORMATION

### Corresponding Authors

\*E-mail: [hugh.doyle@tyndall.ie](mailto:hugh.doyle@tyndall.ie) (H.D.).

\*E-mail: [gareth.redmond@ucd.ie](mailto:gareth.redmond@ucd.ie) (G.R.).

### Notes

The authors declare no competing financial interest.

## REFERENCES

- (1) Janata, J. *Chem. Rev.* **2008**, *108*, 327–328.
- (2) Gardner, J. W.; Yinon, Y. In *NATO Science Series II: Mathematics, Physics and Chemistry*; Kluwer Academic: Dordrecht, 2004.
- (3) Nagarajan, R.; Zukas, W.; Hatton, T. A.; Lee, S. *Nanoscience and Nanotechnology for Chemical and Biological Defense*; ACS Symposium Series; American Chemical Society: Washington, DC, 2009.
- (4) Senesac, L.; Thundat, T. G. *Mater. Today* **2008**, *11*, 28–36.
- (5) Moore, D. S. *Rev. Sci. Instrum.* **2004**, *75*, 2499–2512.
- (6) Meaney, M. S.; McGuffin, V. L. *Anal. Bioanal. Chem.* **2008**, *391*, 2557–2576.
- (7) Toal, S. J.; Trogler, W. C. *J. Mater. Chem.* **2006**, *16*, 2871–2883.
- (8) Germain, M. E.; Knapp, M. J. *Chem. Soc. Rev.* **2009**, *38*, 2543–2555.
- (9) Tao, S. Y.; Yin, J. X.; Li, G. T. *J. Mater. Chem.* **2008**, *18*, 4872–4878.



- (10) Yang, J. S.; Swager, T. M. *J. Am. Chem. Soc.* **1998**, *120*, 11864–11873.
- (11) Le Barny, P. L.; Obert, E. T.; Soyer, F.; Malval, J. P.; Leray, I.; Lemaitre, N.; Pansu, R.; Simic, V.; Doyle, H.; Redmond, G.; Loiseaux, B. *Proc. SPIE Int. Soc. Opt. Eng.* **2005**, 5990, 59900S.
- (12) Bunte, G.; Hürtlen, J.; Pontius, H.; Hartlieb, K.; Krause, H. *Anal. Chim. Acta* **2007**, *591*, 49–56.
- (13) Germain, M. E.; Knapp, M. J. *J. Am. Chem. Soc.* **2008**, *130*, 5422–5423.
- (14) Thomas, S. W.; Joly, G. D.; Swager, T. M. *Chem. Rev.* **2007**, *107*, 1339–1386.
- (15) Östmark, H.; Wallin, S.; Ang, H. G. *Propellants Explos. Pyrotech.* **2012**, *37*, 12–23.
- (16) McQuade, D. T.; Pullen, A. E.; Swager, T. M. *Chem. Rev.* **2000**, *100*, 2537–2574.
- (17) Rochat, S.; Swager, T. M. *ACS Appl. Mater. Interfaces* **2013**, *5*, 4488–4502.
- (18) Diehl, K. L.; Anslyn, E. V. *Chem. Soc. Rev.* **2013**, *42*, 8596–8611.
- (19) FLIR Systems, L. pp FLIR Systems, Inc. Explosives & Narcotics Detection. <http://www.flir.com/threatdetection> (accessed January 20, 2015).
- (20) Zu, B.; Guo, Y.; Dou, X. *Nanoscale* **2013**, *5*, 10693–10701.
- (21) Sirbulu, D. J.; Law, M.; Pauzaskie, P.; Yan, H. Q.; Maslov, A. V.; Knutsen, K.; Ning, C. Z.; Saykally, R. J.; Yang, P. D. *Proc. Natl. Acad. Sci. U.S.A.* **2005**, *102*, 7800–7805.
- (22) Huang, J. X.; Virji, S.; Weiller, B. H.; Kaner, R. B. *J. Am. Chem. Soc.* **2003**, *125*, 314–315.
- (23) Naddo, T.; Che, Y. K.; Zhang, W.; Balakrishnan, K.; Yang, X. M.; Yen, M.; Zhao, J. C.; Moore, J. S.; Zang, L. *J. Am. Chem. Soc.* **2007**, *129*, 6978–6979.
- (24) Che, Y. K.; Yang, X. M.; Loser, S.; Zang, L. *Nano Lett.* **2008**, *8*, 2219–2223.
- (25) Zhao, Y. S.; Wu, J. S.; Huang, J. X. *J. Am. Chem. Soc.* **2009**, *131*, 3158–3159.
- (26) Massuyeau, F.; Duval, J. L.; Athalin, H.; Lorcy, J. M.; Lefrant, S.; Wéry, J.; Faulques, E. *Nanotechnology* **2009**, *20*, 155701.
- (27) Fasano, V.; Polini, A.; Morello, G.; Moffa, M.; Camposeo, A.; Pisignano, D. *Macromolecules* **2013**, *46*, S935–S942.
- (28) Zang, L.; Che, Y. K.; Moore, J. S. *Acc. Chem. Res.* **2008**, *41*, 1596–1608.
- (29) Zhao, Y. S.; Fu, H. B.; Peng, A. D.; Ma, Y.; Liao, Q.; Yao, J. N. *Acc. Chem. Res.* **2010**, *43*, 409–418.
- (30) Zhao, Y. S.; Peng, A. D.; Fu, H. B.; Ma, Y.; Yao, J. N. *Adv. Mater.* **2008**, *20*, 1661–1665.
- (31) McAlpine, M. C.; Ahmad, H.; Wang, D. W.; Heath, J. R. *Nat. Mater.* **2007**, *6*, 379–384.
- (32) Gu, F. X.; Zhang, L.; Yin, X. F.; Tong, L. M. *Nano Lett.* **2008**, *8*, 2757–2761.
- (33) Pagliara, S.; Vitiello, M. S.; Camposeo, A.; Polini, A.; Cingolani, R.; Scamarcio, G.; Pisignano, D. *J. Phys. Chem. C* **2011**, *115*, 20399–20405.
- (34) Cui, Q. H.; Zhao, Y. S.; Yao, J. *Chem. Sci.* **2014**, *5*, 52–57.
- (35) Persano, L.; Camposeo, A.; Pisignano, D. *Prog. Polym. Sci.* **2014**, DOI: 10.1016/j.progpolymsci.2014.1010.1001.
- (36) Ramgir, N. S.; Yang, Y.; Zacharias, M. *Small* **2010**, *6*, 1705–1722.
- (37) Di Benedetto, F.; Camposeo, A.; Pagliara, S.; Mele, E.; Persano, L.; Stabile, R.; Cingolani, R.; Pisignano, D. *Nat. Nanotechnol.* **2008**, *3*, 614–619.
- (38) Huang, Y. W.; Quan, B. G.; Wei, Z. X.; Liu, G. T.; Sun, L. F. *J. Phys. Chem. C* **2009**, *113*, 3929–3933.
- (39) Garreau, A.; Massuyeau, F.; Cordier, S.; Molard, Y.; Gautron, E.; Bertocini, P.; Faulques, E.; Wéry, J.; Humbert, B.; Bulou, A.; Duval, J.-L. *ACS Nano* **2013**, *7*, 2977–2987.
- (40) Zhang, C.; Zhao, Y. S.; Yao, J. *New J. Chem.* **2011**, *35*, 973–978.
- (41) Dawson, K.; Lovera, P.; Iacopino, D.; O’Riordan, A.; Redmond, G. *J. Mater. Chem.* **2011**, *21*, 15995–16000.
- (42) Grell, M.; Bradley, D. D. C.; Ungar, G.; Hill, J.; Whitehead, K. S. *Macromolecules* **1999**, *32*, S810–S817.
- (43) Ariu, M.; Lidzey, D. G.; Sims, M.; Cadby, A. J.; Lane, P. A.; Bradley, D. D. C. *J. Phys.: Condens. Matter* **2002**, *14*, 9975.
- (44) Grell, M.; Bradley, D. D. C.; Long, X.; Chamberlain, T.; Inbasekaran, M.; Woo, E. P.; Soliman, M. *Acta Polym.* **1998**, *49*, 439–444.
- (45) Ariu, M.; Sims, M.; Rahn, M. D.; Hill, J.; Fox, A. M.; Lidzey, D. G.; Oda, M.; Cabanillas-Gonzalez, J.; Bradley, D. D. C. *Phys. Rev. B* **2003**, *67*, 195333.
- (46) Worsfold, O.; Hill, J.; Heriot, S. Y.; Fox, A. M.; Bradley, D. D. C.; Richardson, T. H. *Mater. Sci. Eng., C* **2003**, *23*, 541–544.
- (47) Chunwaschirasiri, W.; Tanto, B.; Huber, D.; Winokur, M. *Phys. Rev. Lett.* **2005**, *94*, 107402.
- (48) Lovera, P.; Redmond, G. *J. Nanosci. Nanotechnol.* **2013**, *13*, S194–S202.
- (49) Khan, A.; Sreearunothai, P.; Herz, L.; Banach, M.; Köhler, A. *Phys. Rev. B* **2004**, *69*, 085201.
- (50) Chen, S. H.; Su, A. C.; Chen, S. A. *J. Phys. Chem. B* **2005**, *109*, 10067–10072.
- (51) Chang, C. P.; Chao, C. Y.; Huang, J. H.; Li, A. K.; Hsu, C. S.; Lin, M. S.; Hsieh, B. R.; Su, A. C. *Synth. Met.* **2004**, *144*, 297–301.
- (52) Janietz, S.; Bradley, D. D. C.; Grell, M.; Giebler, C.; Inbasekaran, M.; Woo, E. P. *Appl. Phys. Lett.* **1998**, *73*, 2453–2455.
- (53) Chen, R.-F.; Zhu, R.; Fan, Q.-L.; Huang, W. *Org. Lett.* **2008**, *10*, 2913–2916.
- (54) Gong, X.; Moses, D.; Heeger, A. J.; Xiao, S. *Synth. Met.* **2004**, *141*, 17–20.
- (55) Ma, W. L.; Iyer, P. K.; Gong, X.; Liu, B.; Moses, D.; Bazan, G. C.; Heeger, A. J. *Adv. Mater.* **2005**, *17*, 274–277.
- (56) Liao, J.-L.; Chen, X.; Liu, C.-Y.; Chen, S.-A.; Su, C.-H.; Sut, A.-C. *J. Phys. Chem. B* **2007**, *111*, 10379–10385.
- (57) Lu, H. H.; Liu, C. Y.; Chang, C. H.; Chen, S. A. *Adv. Mater.* **2007**, *19*, 2574–2579.
- (58) Bai, H.; Shi, G. *Sensors* **2007**, *7*, 267–307.
- (59) Cragin, J. H.; Leggett, D. C. *Diffusion and Flux of Explosive-Related Compounds in Plastic Mine Surrogates*; DTIC Document; DARPA: Arlington, VA, 2003.
- (60) Stoessel, M.; Wittmann, G.; Staudigel, J.; Steuber, F.; Blassing, J.; Roth, W.; Klausmann, H.; Rogler, W.; Simmerer, J.; Winnacker, A.; Inbasekaran, M.; Woo, E. P. *J. Appl. Phys.* **2000**, *87*, 4467–4475.
- (61) van Krevelen, D. W.; te Nijenhuis, K. *Properties of Polymers*, 4th ed.; Elsevier: Amsterdam, 2009.
- (62) Hansen, C. M. *Hansen Solubility Parameters: A User’s Handbook*; CRC Press: Boca Raton, 2007.
- (63) *Handbook of Physical Properties of Organic Chemicals*; CRC Press: Boca Raton, 1997.
- (64) Sheehan, P. E.; Whitman, L. J. *Nano Lett.* **2005**, *5*, 803–807.
- (65) Wegner, G. *Macromol. Chem. Phys.* **2003**, *204*, 347–357.
- (66) Nair, P. R.; Alam, M. A. *Appl. Phys. Lett.* **2006**, *88*, 233120.
- (67) Inglezakis, V. J.; Pouloupoulos, S. G. *Adsorption, Ion Exchange and Catalysis: Design of Operations and Environmental Applications*; Elsevier Science: Amsterdam, The Netherlands, 2006.
- (68) Walczak, R.; Dziuban, J.; Szczepańska, P.; Scholles, M.; Doyle, H.; Krüger, J.; Ruano-Lopez, J. *Procedia Chem.* **2009**, *1*, 999–1002.
- (69) Wei, Q.; Qi, H.; Luo, W.; Tseng, D.; Ki, S. J.; Wan, Z.; Göröcs, Z.; Bentolila, L. A.; Wu, T.-T.; Sun, R.; Ozcan, A. *ACS Nano* **2013**, *7*, 9147–9155.
- (70) Wei, Q.; Luo, W.; Chiang, S.; Kappel, T.; Mejia, C.; Tseng, D.; Chan, R. Y. L.; Yan, E.; Qi, H.; Shabbir, F.; Ozkan, H.; Feng, S.; Ozcan, A. *ACS Nano* **2014**, *8*, 12725–12733.
- (71) Wei, Q.; Nagi, R.; Sadeghi, K.; Feng, S.; Yan, E.; Ki, S. J.; Caire, R.; Tseng, D.; Ozcan, A. *ACS Nano* **2014**, *8*, 1121–1129.
- (72) Ming, K.; Kim, J.; Biondi, M. J.; Syed, A.; Chen, K.; Lam, A.; Ostrowski, M.; Rebbapragada, A.; Feld, J. J.; Chan, W. C. W. *ACS Nano* **2015**, DOI: 10.1021/nn5072792.